



Article

Space-Based Mapping of Pre- and Post-Hurricane Mangrove Canopy Heights Using Machine Learning with Multi-Sensor Observations

Boya Zhang ^{1,2,3,*}, Daniel Gann ⁴, Shimon Wdowinski ¹, Chaohao Lin ⁵, Erin Hestir ², Lukas Lamb-Wotton ⁶, Khandker S. Ishtiaq ⁷, Kaleb Smith ⁸ and Yuepeng Li ⁹

- ¹ Institute of Environment, Department of Earth and Environment, Florida International University, Miami, FL 33199, USA
- Department of Civil & Environmental Engineering, University of California at Merced, Merced, CA 95340, USA
- School of the Environment, Yale University, New Haven, CT 06501, USA
- Institute of Environment, Department of Biological Sciences, Florida International University, Miami, FL 33199, USA; gannd@fiu.edu
- Department of Electrical and Computer Engineering, Florida International University, Miami, FL 33174, USA
- 6 Department of Earth and Environmental Sciences, Tulane University, New Orleans, LA 70118, USA
- ⁷ The Everglades Foundation, Palmetto Bay, FL 33157, USA
- ⁸ NVIDIA, Santa Clara, CA 95051, USA
- Ocastal Research Lab, International Hurricane Research Center, Florida International University, Miami, FL 33199, USA; yuepli@fiu.edu
- * Correspondence: boya.zhang@yale.edu

Abstract: Coastal mangrove forests provide numerous ecosystem services, which can be disrupted by natural disturbances, mainly hurricanes. Canopy height (CH) is a key parameter for estimating carbon storage. Airborne Light Detection and Ranging (LiDAR) is widely viewed as the most accurate method for estimating CH but data are often limited in spatial coverage and are not readily available for rapid impact assessment after hurricane events. Hence, we evaluated the use of systematically acquired space-based Synthetic Aperture Radar (SAR) and optical observations with airborne LiDAR to predict CH across expansive mangrove areas in South Florida that were severely impacted by Category 3 Hurricane Irma in 2017. We used pre- and post-Irma LiDAR-derived canopy height models (CHMs) to train Random Forest regression models that used features of Sentinel-1 SAR time series, Landsat-8 optical, and classified mangrove maps. We evaluated (1) spatial transfer learning to predict regional CH for both time periods and (2) temporal transfer learning coupled with species-specific error correction models to predict post-Irma CH using models trained by pre-Irma data. Model performance of SAR and optical data differed with time period and across height classes. For spatial transfer, SAR data models achieved higher accuracy than optical models for post-Irma, while the opposite was the case for the pre-Irma period. For temporal transfer, SAR models were more accurate for tall trees (>10 m) but optical models were more accurate for short trees. By fusing data of both sensors, spatial and temporal transfer learning achieved the root mean square errors (RMSEs) of 1.9 m and 1.7 m, respectively, for absolute CH. Predicted CH losses were comparable with LiDAR-derived reference values across height and species classes. Spatial and temporal transfer learning techniques applied to readily available spaceborne satellite data can enable conservation managers to assess the impacts of disturbances on regional coastal ecosystems efficiently and within a practical timeframe after a disturbance event.

Keywords: mangrove; canopy height; data fusion; machine learning; transfer learning; natural disturbance; hurricane



Citation: Zhang, B.; Gann, D.; Wdowinski, S.; Lin, C.; Hestir, E.; Lamb-Wotton, L.; Ishtiaq, K.S.; Smith, K.; Li, Y. Space-Based Mapping of Pre- and Post-Hurricane Mangrove Canopy Heights Using Machine Learning with Multi-Sensor Observations. *Remote Sens.* **2024**, *16*, 3992. https://doi.org/10.3390/ rs16213992

Academic Editor: Jose Moreno

Received: 16 August 2024 Revised: 15 October 2024 Accepted: 24 October 2024 Published: 28 October 2024



Copyright: © 2024 by the authors. Licensee MDPI, Basel, Switzerland. This article is an open access article distributed under the terms and conditions of the Creative Commons Attribution (CC BY) license (https://creativecommons.org/licenses/by/4.0/).

Remote Sens. 2024, 16, 3992 2 of 21

1. Introduction

Mangrove forests grow along low elevation tropical and subtropical coastlines, providing valuable ecosystem services, including storm protection and shoreline stabilization, with carbon sequestration rates that are three to four times greater per unit area than other tropical forests [1–3]. However, global mangrove coverage has decreased since 1980 by 20–35%, which is attributed to human activity (e.g., deforestation, coastal development) and natural factors (e.g., sea-level rise, shoreline erosion, hurricanes, droughts) [4,5] and more than half of all mangrove ecosystems face the risk of collapse by 2050 [6]. Since mangrove forests are mostly located in coastal regions, they are particularly vulnerable to hurricanes, which account for ~11% of global mangrove losses and die-offs [7–11]. Quantifying the initial loss and recovery rates of mangrove forests is crucial for understanding the impacts on the ecosystem structure, function, and the services provided by mangroves.

Canopy height (CH) is a critical parameter in estimating changes in the aboveground biomass of mangroves when applying allometric equations [12]. Mangrove CH measured in the field at regional scales is impractical, and thus has been estimated using remote sensing methods including airborne and spaceborne laser scanning, also referred to as Light Detection and Ranging (LiDAR) [13–15], optical imaging [10], and Synthetic Aperture Radar (SAR) [8,16].

LiDAR scanning is an active remote sensing technique that emits pulses toward the Earth's surfaces and receives the backscattered pulse returns from different vertical layers of scanned vegetation canopies [17]. Spaceborne LiDAR provides vegetation structure information at global coverage, but the large footprint size and non-exhaustive data acquisition design limit its applications [18,19]. Airborne LiDAR Scanning (ALS) is viewed as the most accurate sensor for CH prediction, but studies tend to focus on a single period for local area applications due to the high cost and limited spatial coverage [20]. Full areal coverage of entire landscapes after large disturbance events such as hurricanes is prohibitively expensive and requires long planning and data processing times before assessments can be made. Not knowing when and where a natural disturbance event occurs makes planning ALS missions difficult to capture CH loss information, which explains why only a few studies have applied multi-temporal LiDAR measurements to evaluate CH loss caused by disturbances [15,21].

To gain a deeper understanding of mangrove dynamics in response to natural disturbances at a regional scale, it is therefore imperative to develop methods that can use data that are captured systematically over large spatial extents at high temporal frequency so that they are readily available immediately before and after natural disasters occur. Spaceborne optical and SAR sensors have become prevalent for studying mangrove canopy dynamics by harnessing the high temporal resolution and global coverage [22–24]. Data from both optical and SAR sensors provide complementary information on the physical characteristics of vegetation. Optical indices capture foliage and defoliation characteristics and have been successfully applied to evaluate the phenology of mangrove forests and damage following cyclones [24,25], whereas changes in woody biomass (e.g., loss of branches) are not directly captured. SAR backscatter data better capture physical properties related to tree branches and trunks and are useful for assessing changes in vegetation structure because the microwave energy can penetrate foliage and reflect off woody plant components [26–28].

Hence, multi-sensor data fusion, combining data from different types of sensors to leverage their complementary strength, has successfully predicted CH using regression models [29], machine learning (ML) such as Random Forest (RF) [16,30], Decision Tree [19], Support Vector Machine (SVM) [31], and Deep Learning (DL) Neural Network methods [18,32,33]. However, there remain knowledge gaps in the current status of data fusion.

First, few studies have explored the complementary properties of SAR and optical data for canopy height (CH) prediction before and after natural disturbances, primarily due to the scarcity of ground reference data. Additionally, there is little knowledge of how

Remote Sens. 2024, 16, 3992 3 of 21

both sensor types perform across the range of CH values, e.g., which sensor is better suited for accurately measuring taller mangroves.

Second, most data fusion studies focused on spatial transfer learning, i.e., training a model using labeled remote sensing imagery from a specific geographic area and applying the model to other areas with limited labeled data. However, fewer studies have explored temporal transfer learning, where the model is trained using historic data and applied to a different period [34,35]. Temporal transfer learning is particularly important for natural resource managers to evaluate the impacts induced by natural disturbances within a practical timeframe. However, accurate temporal transfer learning is difficult due to significant changes in the mangrove structure and changes in materials on the ground (e.g., dead woody debris) [28].

Third, most studies used the temporal median/mean of SAR backscatter as predictor variables, which compresses the information of temporal variations [18]. SAR backscatter in inundated mangrove areas varies in response to changes in water level variations (e.g., high tides and low tides, [36,37]), and using a single SAR backscatter image could lead to bias in CH prediction. To our knowledge, no studies have been published using SAR time series to evaluate CH changes due to natural disturbances.

This study used pre- and post-disturbance CH data derived from Goddard's LiDAR, Hyperspectral & Thermal Imager (G-LiHT) airborne sensor as reference to train RF models for predicting CH from SAR, optical, and mangrove class features. The RF models were trained for (1) spatial transfer learning for pre- and post-disturbance periods and (2) temporal transfer learning that predicts post-disturbance CH using models calibrated by pre-disturbance data. To fill the knowledge gaps, this study addresses the following questions: For spatial transfer learning, how does the accuracy of SAR and optical data models vary between pre- and post-disturbance periods? For spatial and temporal transfer learning, how does the accuracy of absolute CH resulting from SAR and optical models vary across CH height classes? Does a SAR time series achieve higher accuracy than using a single SAR backscatter observation? How does the accuracy of canopy height loss vary with mangrove species and canopy height?

2. Study Area and Data Preparation

This section first describes the study area in South Florida (Section 2.1) and the 2017 Hurricane Irma event, which had a significant impact on the mangrove ecosystem (Section 2.2). Next, we introduce the data preparation process for each of the four types of geospatial data that were used for the spatial and temporal transfer learning models (Section 2.3).

2.1. Study Area

Our study area, located along the southwestern coast of Florida (Figure 1a), covers 1296 km² of mangrove-dominated vegetation within Everglades National Park (ENP) [10], the largest contiguous protected mangrove forests in the continental USA ([8], Figure 1b). The distribution of mangroves species within ENP varies with inundation frequency and depth and historical hurricane disturbance events (Figure 1c, [38–40]). Mixed mangrove assemblages dominate along the coastline and are more frequent than single-species communities (Figure 1c). Previous studies successfully modelled regional CH values in 2000–2004 [8], 2011–2014 [41], and March 2017 [32], all of which showed a similar spatial pattern of CH distribution. Downstream along the Harney River, mangrove forests are dominated by a mixed-species assemblage with relatively tall CH (Figure 1f,g). In the Ten Thousand Islands and Flamingo sites, forests tend to be dominated by mixed-species and black mangrove with intermediate heights (Figure 1l,m,o,p), and upstream, particularly along Shark River, short red mangroves tend to dominate (Figure 1i,j).

Remote Sens. 2024, 16, 3992 4 of 21

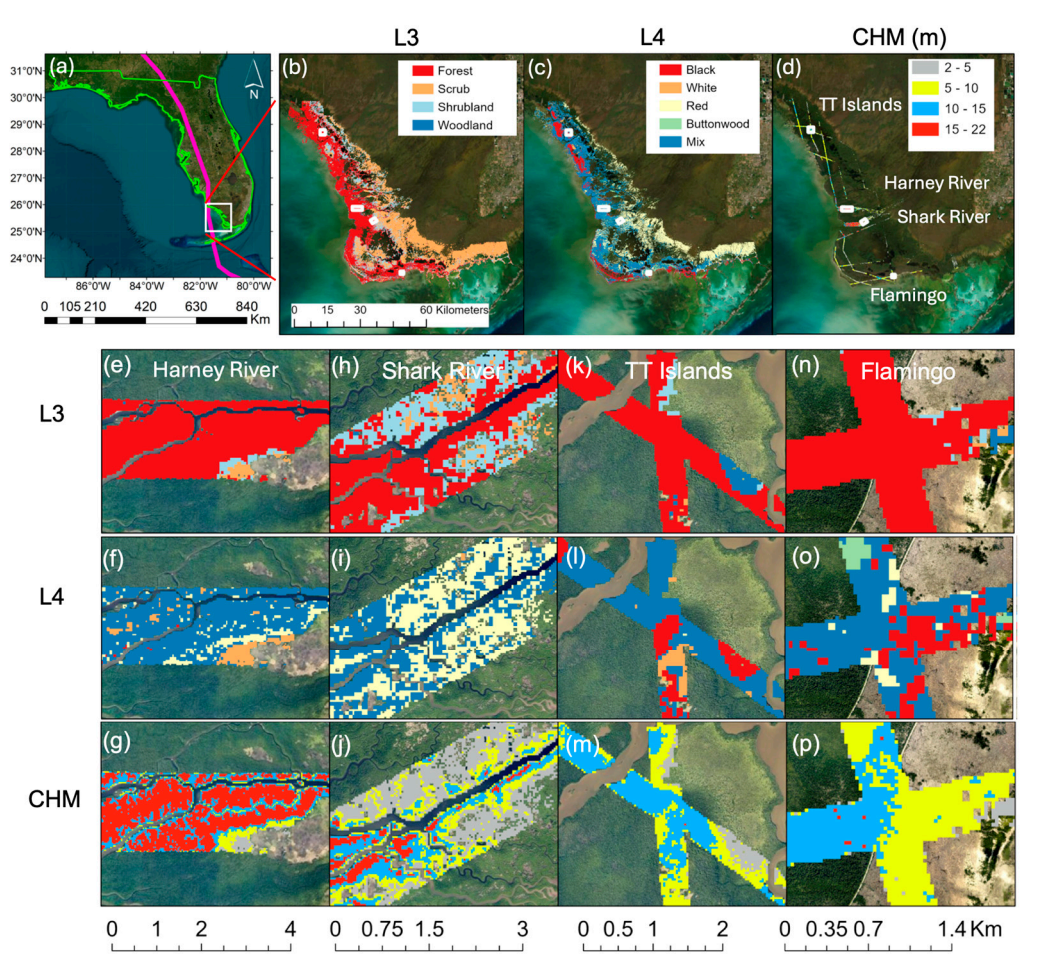


Figure 1. (a) Florida state boundary and Hurricane Irma track. (b) Level 3 mangrove classification map. (c) Level 4 mangrove species classification. (d) The 30 m G-LiHT footprint of pre-Irma CHM. (e–p) Zoom-in views for four representative sites.

2.2. Disturbance Event

Coastal mangroves were significantly impacted by Hurricane Irma that approached South Florida on 10 September 2017, as a category 3 cyclone with maximum sustained winds of ~50 m/s (112 mph) ([15], wind map displayed in Figure S1). Strong wind and storm surge flooding caused various degrees of damage to mangroves, including defoliating canopies, breaking stems and branches, and uprooting entire trees. The degree of impact and damage depends on the physical characteristics of the storm (e.g., wind velocity), the height and condition of the vegetation, and the location of affected vegetation relative to the hurricane's path and wind fields [42]. Since the track of Hurricane Irma stayed offshore (Figure 1a), tall mangrove trees at downstream locations close to the coastline (e.g., Harney River, Ten Thousand Islands, Flamingo locations in Figure 1) experienced the greatest impact of canopy loss, whereas inland mangroves (e.g., upstream Shark River in Figure 1) were less impacted [10].

2.3. Data and Data Processing

This study relied on four types of geospatial datasets to train and apply transfer models to predict CH over large regions. G-LiHT LiDAR CHM served as reference label height information, and Sentinel-1 dual-polarized SAR backscatter, Landsat-8 multispectral optical images, and categorical mangrove maps were used as feature variables to train CH models. We prepared two datasets for pre- and post-Irma time windows with the same spatial coverage, each consisting of label and feature variables (Figure 2). All data were projected to Universal Transverse Mercator (UTM Zone 17N), using World Geodetic System

Remote Sens. **2024**, 16, 3992 5 of 21

1984 (WGS-84) and Earth Gravitational Model 1996 (EGM96) as the horizontal and vertical datum, respectively.

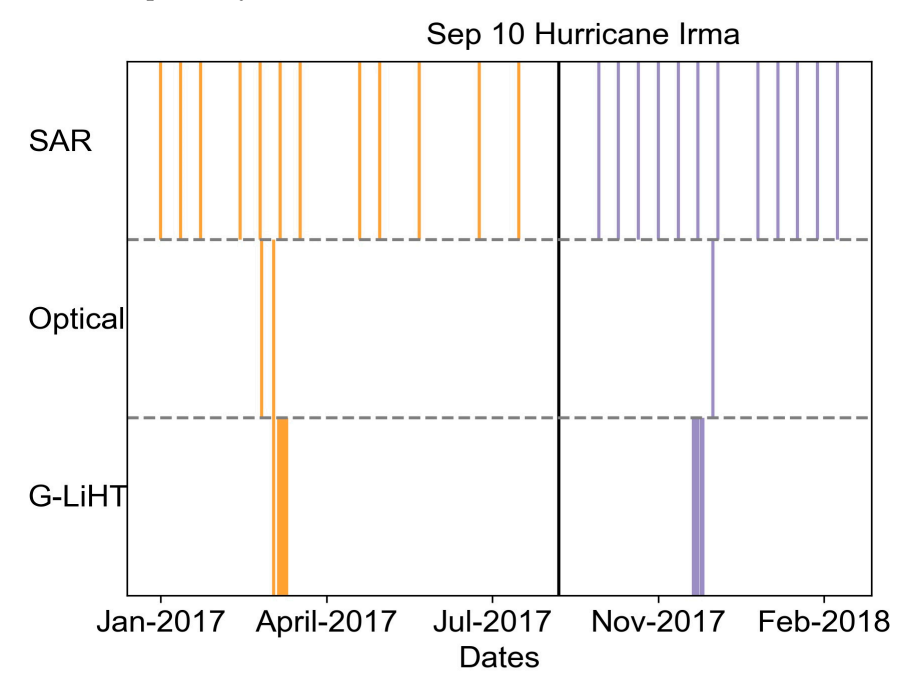


Figure 2. Timeline of pre-Irma (orange lines) and post-Irma (purple lines) observations separated by September 2017 Hurricane Irma (the dark vertical line).

2.3.1. Reference Canopy Height Model

G-LiHT is a National Aeronautics and Space Administration (NASA) airborne imaging system that simultaneously collects LiDAR, hyperspectral imagery, and thermal data to map the composition, structure, and function of terrestrial ecosystems [43]. G-LiHT data across South Florida were collected between 22 and 30 March 2017, six months before Hurricane Irma, and a post-Irma survey campaign between November 30 to December 6, 2017 (three months after Irma). Both campaigns used the same sensor configurations, acquiring data for over 130,000 ha of mangrove forests [10,44]. The raw LiDAR data were processed by NASA who provided access to CHMs at G-LiHT data center (https://glihtdata.gsfc.nasa.gov/, accessed on August 2022). We obtained 1758 pre-Irma and 1491 post-Irma CHM datasets. For its scale compatibility with SAR and optical observations, we resampled the 1 m resolution CHMs to the 30 m Landsat grid by calculating the mean of CH for each 30×30 m pixel (Figure 1d).

2.3.2. Vegetation Cover and Mangrove Classes

The 2012 National Park Service (NPS) vegetation cover map [45] contains seven levels of increasingly detailed vegetation information of Everglades National Park. Vegetation labels were applied to 50 × 50 m grid cells based on 2009 color-infrared aerial imagery with an accuracy of 89.2% [45]. As there were no hurricanes significantly impacting the study area between 2009 and 2017, the vegetation cover map was valid for this study [11]. We subset the NPS vegetation cover map to locations classified as mangroves and used two 50 m resolution classification maps at different class information levels for two purposes. The Level 3 (L3) classification with general classification scheme, including four classes "Mangrove Forest", "Mangrove Scrub", "Mangrove Shrubland", and "Mangrove Woodland" (Figure 1b), was used for model training and evaluation. The Level 4 (L4) finer class-level map that provides mangrove species identifiers was used to assess whether differences in model prediction accuracies existed among different species (Figure 1c). The mangrove species classes included (1) *Avicennia germinans* (black mangrove), (2) *Laguncularia racemosa* (white mangrove), (3) *Rhizophora mangle* (red mangrove), (4) *Conocarpus erectus* (button-

Remote Sens. 2024, 16, 3992 6 of 21

wood), and (5) a mixed-species mangrove class. We extracted both L3 and L4 information at center points of 30 m grid cells of Landsat 8 images.

2.3.3. SAR Backscatter

For pre- and post-Irma periods, we used 12 contiguous Sentinel-1A C-band dual-polarized (VV and VH polarization bands) SAR acquisitions (Figure 2). The pre-Irma time series from January 2017 to August 2017 and the post-Irma time series from October 2017 to February 2018 were acquired from the Alaska Satellite Facility (https://search.asf.alaska.edu/#/, accessed on May 2021). The acquired SAR data were Level 1 high-resolution Ground Range Detected (GRD) Interferometric Wide (IW) mode products with a spatial resolution of 20 m \times 22 m in range and azimuth directions, respectively. We processed the GRD data using the Sentinel Application Platform (SNAP,) by following the standard procedure [46] including thermal noise removal, radiometric calibration, speckle filtering using Lee filter with a 7 \times 7 window, and range-Doppler terrain correction using 3-arcsecond Shuttle Radar Topography Mission (SRTM). The output images were resampled to 30 m using a bilinear interpolation method to reduce speckle effects [47] and co-registered with the Landsat-8 grid cells. Pixel values of the images were backscatter coefficients (σ^0), also referred to as sigma nought, in decibel (dB) units.

For each period, 12 contiguous SAR acquisitions were evenly distributed before and after the corresponding G-LiHT acquisition dates (Figure 2). The pre-Irma time series spans a longer period than post-Irma because there were more data gaps in early- and mid-2017 compared to late 2017 (Figure 2). We assumed that mangrove CH did not significantly change within each time window. The assumption is more valid for the pre-Irma period when mangrove growth form was relatively stable. For the post-Irma period, the period used to define the post-Irma period needed to be long enough to build a backscatter time series that incorporated tidal variability, but short enough to represent changed canopy conditions. Although epicormic growth led to CH increase, the mangrove canopy remained largely open up to 9 months after Hurricane Irma because of extensive branch damage [48].

2.3.4. Multispectral Optical Data

We used Landsat-8 Collection 2 Tier 1 calibrated top-of-atmosphere (TOA) reflectance from Google Earth Engine (GEE). We selected Landsat-8 images with the least cloud coverage for each of the two periods. To achieve full spatial coverage, we mosaicked 15 and 22 March 2017 images representing the pre-Irma period, and used the 12 December 2017 image for the post-Irma period (Figure 2). We used the algorithm provided by GEE to remove cloud-covered pixels [49]. We selected ten optical variables that were previously found useful for detecting mangrove canopy dynamics and predicting CH [18,22], including red, green, blue, near-infrared, two shortwave infrared bands (corresponding to band two to seven of the Landsat-8 products, or B2–B7), and four derived spectral indices, including Normalized Difference Vegetation Index (NDVI), Normalized Difference Moisture Index (NDMI), Soil Adjusted Vegetation Index (SAVI), and Water Adjusted Vegetation Index (WAVI). The formulas for the index calculations are shown in Table 1.

 Table 1. Formulas and sources of optical indices used for CH prediction.

Index	Equation	Reference
NDVI	NIR-RED NIR+RED	[50]
NDMI	NIR-SWIR1 NIR+SWIR1	[51]
SAVI	$\frac{NIR-RED}{NIR+RED+L} \times (1+L)$	[52]
WAVI	$\frac{NIR-BLUE}{NIR+BLIIE+I} \times (1+L)$	[53]

NIR, RED, BLUE, and SWIR denote near-infrared, red, blue, and shortwave infrared bands, respectively; L is a constant value of 0.5 for Landsat 8 according to [53].

Remote Sens. 2024, 16, 3992 7 of 21

3. Methodology

We trained RF models for spatial and temporal transfer learning to predict the CH of mangrove trees. The RF model was selected because in a test analysis study, it outperformed six other models that included multiple linear regression, decision tree regression, gradient boosting, support vector machine, stacking ensemble, and neural network. The methodology and results of the six models are summarized in Note S1 and Table S1. This section first describes the data preparation steps for the RF model (Section 3.1), followed by model descriptions (Section 3.2), training, and evaluation methods (Section 3.3).

3.1. Data Preparation for the Machine Learning Model

We termed the original dataset covering the entire study area "DS0", including feature and label variables. For both time periods, every pixel was assigned a label of either a valid CHM value (Figure 1d) or "NaN". We conducted two levels of data filtering to remove invalid data from "DS0" (Figure 3a). First, we filtered the pixels with valid feature values to generate the "DS1_pre" and "DS1_post" datasets by masking missing values due to cloud cover for the optical images. We further filtered the pixels with CHM values greater than 2 m corresponding to the CH of mangrove species and intersected the filtered pre-Irma and post-Irma datasets to obtain the common pixels, which was termed "DS2". The DS2 dataset consisted of "DS2_pre" and "DS2_post", which shared the same locations of pixel samples but with different feature and label values. We primarily used the DS2 dataset for the spatial and temporal transfer learning and DS1 was only used for spatial transfer learning to predict CH for the regional mangrove area (Figure 3).

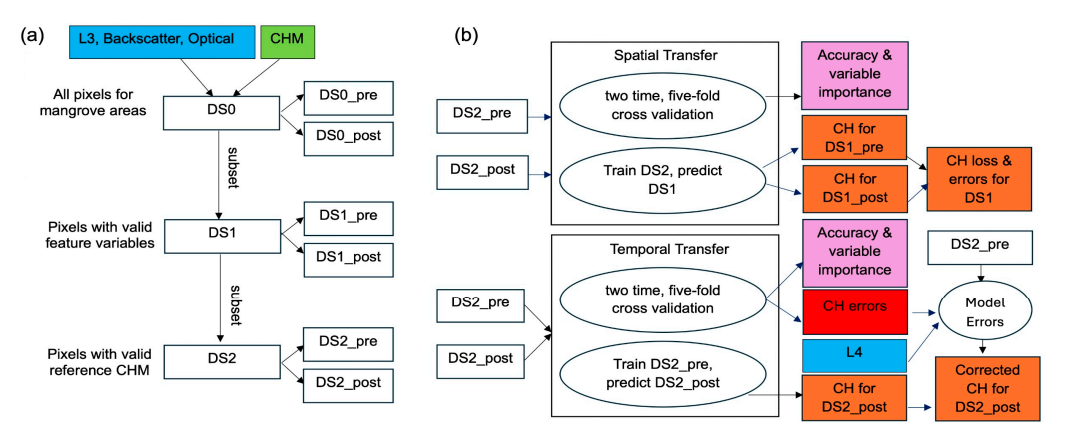


Figure 3. (a) Flow chart of data filtering. (b) Spatial and temporal transfer learning based on *DS2_pre* and *DS2_post* data that are separately used in the spatial transfer but collectively used in the temporal transfer learning. Blue and green rectangles are input variables; white and red rectangles are intermediate products; ovals indicate model processes; pink and orange rectangles are output products.

3.2. Random Forest Model Training and Evaluation for CH Predictions

Random Forest, an ensemble decision tree method, is efficient in both classification and regression problems with non-linear relationships between feature and label variables [54]. We trained RF regression models using the caret package in R (version 6.0.93, [55]) with "ntree" parameter, the number of decision trees set to the default values of 500, and "mtry" parameter, the number of variables randomly collected to be sampled at each split time, set to the default value as the square root of the number of feature variables.

3.3. Spatial Transfer Learning

Spatial transfer learning was conducted for each period separately using two sets of model configurations (Figure 3b). The first configuration trained the model by stratified random sampling 80% of pixels from the DS2 dataset distributed evenly across four L3 classes and evaluated the model with the remaining 20% of pixels. We conducted two-time,

Remote Sens. 2024, 16, 3992 8 of 21

five-fold cross-validation, resulting in ten test sets. We performed independent training and evaluation with: (1) backscatter time series, (2) optical data, and (3) a mix of backscatter and optical data. We also used (1) mean backscatter across the temporal domain, and (2) the backscatter acquisition closest to G-LiHT campaigns for comparison. Each of the feature sets also included L3 classification as a feature variable. For each cross-validation dataset, pre-Irma and post-Irma model configurations shared the same training and evaluation pixels for comparison of results. We systematically compared the performance of SAR and optical data between pre- and post-Irma periods across four height classes: 2–5 m, 5–10 m, 10–15 m, and 15–20 m using Root Mean Squared Error (RMSE) and R squared (R²). Using the evaluation dataset of cross-validations, we quantified the errors of predicted CH loss in response to height and species classes. We assessed canopy height (CH) losses across different height and species classes by calculating the ratio of mean loss errors to mean referenced CH loss. If this ratio was less than 20%, then the predicted CH loss was accurate enough to represent the actual impacts. We calculated the Variable Importance (VI) metric for each variable using percentage increase in mean square error (%IncMSE) [56].

For the second configuration, we trained a model for each period using the feature set that achieved the highest accuracy based on the first model configuration. We used all pixels, respectively, in *DS2_pre* and *DS2_post* to train the models, and predicted CH in the *DS1_pre* and *DS1_post* datasets covering the full extent of mangrove areas using their feature variables. We then predicted CH change by subtracting post-Irma CH from pre-Irma values and validated the results using the reference LiDAR CHM products.

3.4. Temporal Transfer Learning

Temporal transfer learning trained a model using the *DS2_pre* dataset to predict CH for the *DS2_post* dataset because pre-Irma includes a wider range of height values with taller mangroves than post-Irma. When using the post-Irma for training, the high-end range of pre-Irma CH values was not covered and led to underestimation. Similarly, temporal transfer learning included two sets of model configurations (Figure 3b). The first configuration conducted two-time, five-fold cross-validation by stratified random sampling 80% of pixels in *DS2_pre* across the L3 classes for training and using the same pixel locations in *DS2_post* for evaluation. Similarly, we compared the performance of backscatter time series, optical data, and a mix of both. Results from backscatter time series were compared with (1) a temporal mean and (2) a single backscatter closest to the G-LiHT campaign. For each mangrove species according to L4 class, we applied a linear regression model to correct prediction errors as a function of pre-Irma CH (Figure 3b).

The second configuration trained a model using all the pixel samples in *DS2_pre* to predict CH for *DS2_post*. Predictions were exclusively applied to pixels in *DS2* areas. We evaluated CH loss accuracy across height classes and selected the feature set with the most accurate predictions as the results.

4. Results

4.1. Filtered Datasets for Spatial and Temporal Transfer Learning

The DS0 dataset that covers all mangrove locations consisted of 1,440,185 pixels (an equivalent of ~1296.2 km², Figure 1b). The four classes in L3 ("Mangrove Forest", "Mangrove Scrub", "Mangrove Shrubland", and "Mangrove Woodland") occupied 45.9%, 35.3%, 17.4%, and 1.4% of the full area in DS0, respectively (Figure 1b) and the CH values' distribution is provided in Figure S2. First level data filtering resulted in 1,407,415 pixels for the pre-Irma ($DS1_pre$) and 1,403,385 pixels for the post-Irma time period ($DS1_post$), with only 2% and 3% of pixels removed. The second level of data filtering resulted in 133,207 pixels for pre-Irma (Figure 1d), 137,272 pixels for post-Irma with CHM values, and 119,246 common pixels in both time periods as DS2, covering 8% of total areas.

The mean CH decreased after the hurricane for all L4 mangrove species classes (Figure 4a). We selected a representative pixel for each species to illustrate the change in feature values before and after Irma. For the "Black Mangrove", "White Mangrove",

Remote Sens. 2024, 16, 3992 9 of 21

"Red Mangrove", and "Mixed Mangrove" classes, we selected a pixel with pre-Irma height over 10 m and CH loss over 4 m. For "Buttonwood", no tall CH samples were available, and we selected a pixel with short CH and only 1 m of CH loss as an example with less severe impacts. The first four pixels with high CH loss showed that backscatter values increased, but optical index values decreased after the hurricane (Figure 4b), whereas the "Buttonwood" pixel showed less changes in SAR and optical feature values. A systematic comparison of SAR and optical feature values before and after Hurricane Irma is provided in Figure S3. We used all available feature variables for both transfer learning models because removing any of the variables led to lower accuracy.

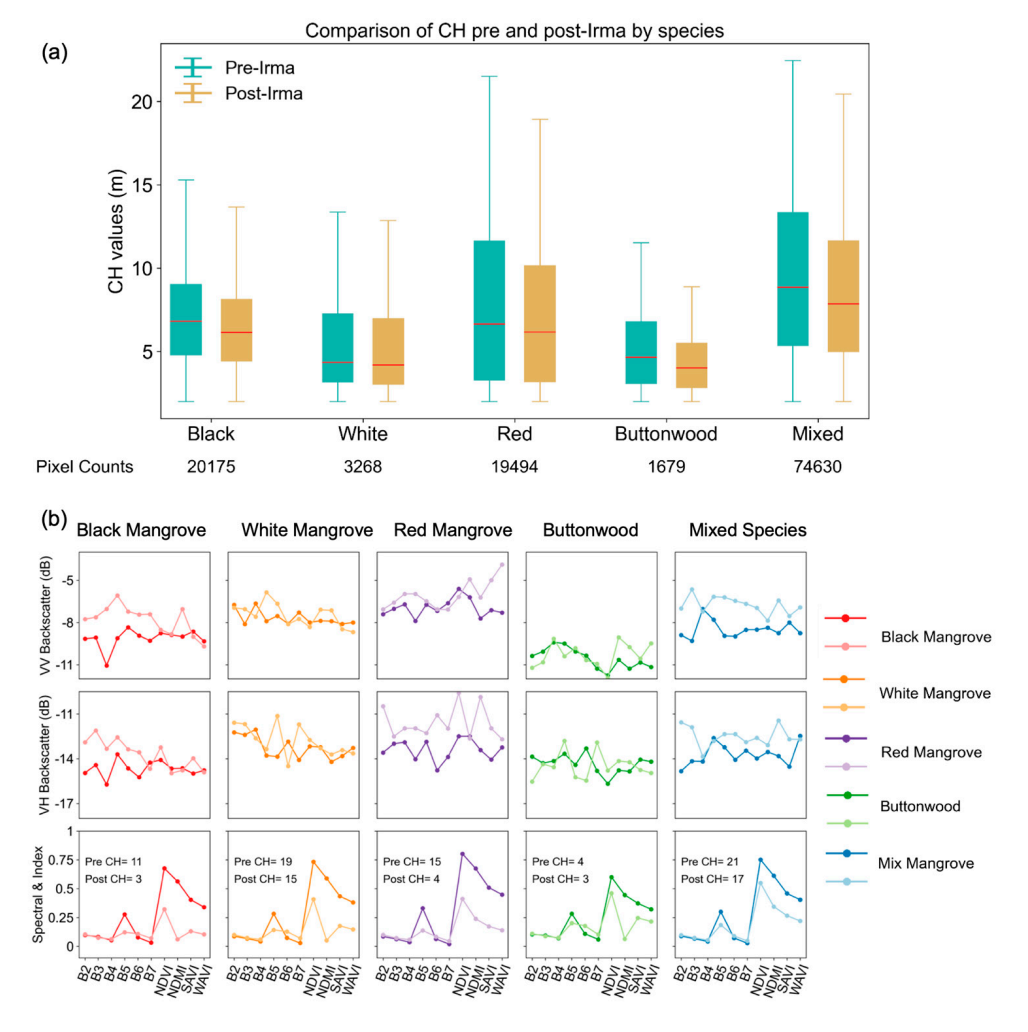


Figure 4. (a) Boxplots for the reference pre- and post-Irma CHM from *DS2* dataset. Red line indicates the median value; the boxes represent the interquartile range between the first quartile (25th percentile) and the third quartile (75th percentile); the whiskers extend from the edges of the box to the smallest and largest values within 1.5 times the interquartile range. (b) Comparison of backscatter time series and optical observations using a representative pixel from each species. For each subplot, darker color represents pre-Irma values and lighter color post-Irma values. CH values are displayed in the last row.

4.2. Results of Spatial Transfer Learning for CH Predictions

4.2.1. Comparison of CH Prediction Accuracy Between SAR and Optical Datasets

Comparing SAR and optical data performance for CH prediction using evaluation datasets showed SAR variables resulted in lower accuracy than optical features for pre-Irma, but higher accuracy than optical features for post-Irma, particularly for tall mangroves over 10 m (Tables 2 and 3). The uncertainty of predictions increased in response to the increase in height values (Table 3). Mixed features achieved an RMSE of 1.9 m and 1.8 m for pre-

and post-Irma periods, respectively, more accurate than using SAR or optical alone (Table 2 and Figure 5a). Prediction uncertainties did not vary significantly among species classes (Figure S4). When using the mean backscatter values with optical observations and L3 vegetation information, the model achieved an RMSE of 2.0 m for both periods. Using the SAR observation closest to the LiDAR campaigns with optical and L3 features resulted in an RMSE of 2.1 m and 1.8 m for the two periods. In both cases, the accuracy was slightly lower than using the backscatter time series with optical and L3 features (1.9 and 1.8 m).

Table 2. Summary of mean and standard deviation of accuracy parameters among cross-validation evaluation datasets for pre- and post-Irma periods.

Sensors	Pre-Irma		Post-Irma		
	RMSE (m)	R ²	RMSE (m)	R ²	
SAR	2.9 ± 0.0	0.6 ± 0.0	2.2 ± 0.0	0.7 ± 0.0	
Optical	2.2 ± 0.0	0.8 ± 0.0	2.4 ± 0.0	0.6 ± 0.0	
Mix	1.9 ± 0.0	0.8 ± 0.0	1.8 ± 0.0	0.8 ± 0.0	

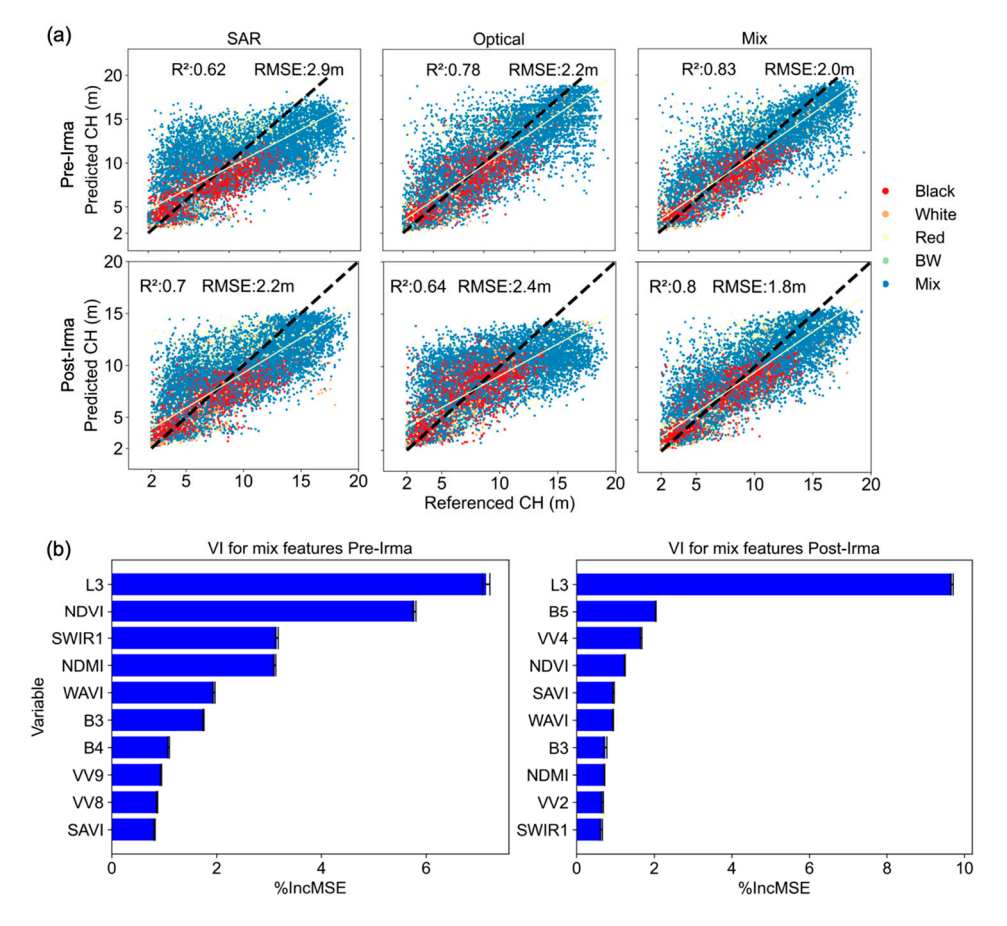


Figure 5. (a) Scatter plot of predicted and referenced CH for pre- and post-Irma from one of the cross-validation evaluation datasets. The yellow lines mark the least-square linear regression model. "BW" in the legend indicates "buttonwood" species. (b) Mean and standard deviation of variable importance of top ten variables using the mixed feature.

Pre-Irma CH (m)	Pre-Irma		Post-Irma			
	SAR	Optical	Mix	SAR	Optical	Mix
2–5 m	2.5	1.8	1.6	2.0	2.0	1.6
5–10 m	2.7	2.2	1.9	2.0	2.0	1.6
10–15 m	2.3	2.2	1.9	2.3	2.6	2.0
15–20 m	4.4	2.8	2.5	3.9	5.0	3.1

Table 3. CH prediction RMSE (m) in response to height classes.

Differences existed for the variable importance ranking from the mixed features between the two periods (Figure 5b). Overall, L3 classification had the highest importance for both periods. Among the optical variables, NDVI stood out with a high percentage increase in mean square error (%IncMSE) values. Some of the SAR features (e.g., VV4) showed high importance for post-Irma, but had low ranking for the pre-Irma period. VV backscatter variables were consistently more important than VH for both periods.

4.2.2. Canopy Height Errors and CH Loss Predictions

Prediction errors (predicted—reference values) from a representative model evaluation dataset showed a linear relationship with reference CH for each mangrove species class (Figure 6). The model overestimated CH for short mangroves and underestimated for tall mangroves across all species. The slope values of the linear regression models were comparable across both periods for each species. The mixed-species class displayed intermediate slope values among the other species. The percentage errors, defined as the ratio of errors to reference height values, were significant for shorter mangroves but progressively diminished to nearly zero as the CH increased.

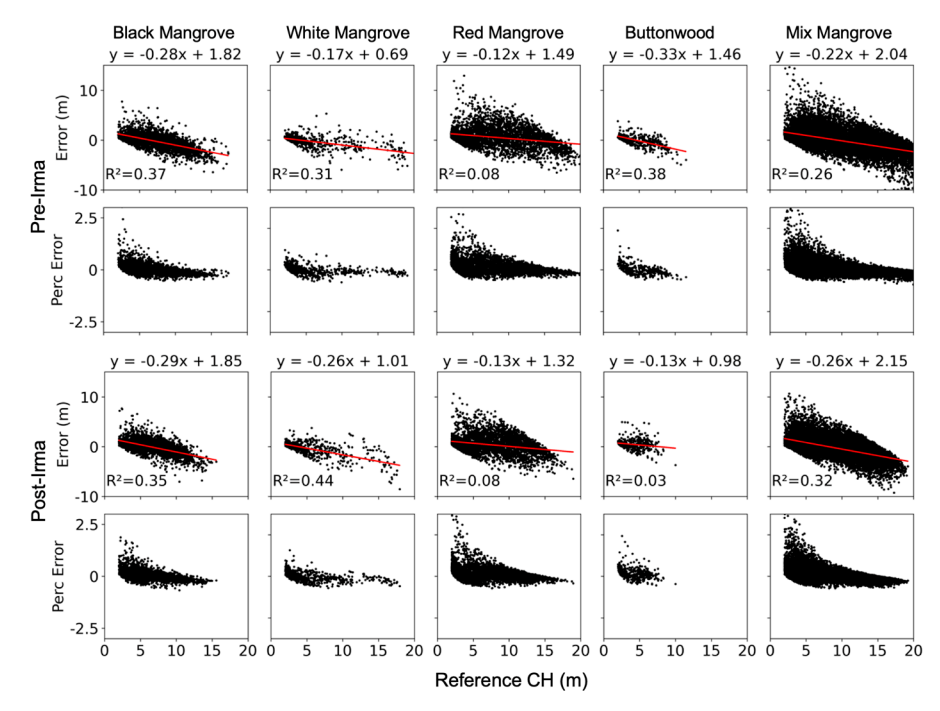


Figure 6. Scatter plots of prediction error and percentage (Perc) error versus reference CH for both time periods by species. Red lines are the least-squared linear models.

Our results showed that tall pre-Irma mangroves experienced greater CH losses than short mangroves (Figure 7c). Mean and standard deviation values of CH losses from all evaluation datasets were comparable between predicted and reference datasets across height and species classes (Figure 7d). The only exception was buttonwood with large errors or no samples for the three height classes over 5 m. In most cases, the ratios of mean

errors to mean referenced CH loss were less than 20%, satisfying our criteria, except for some species classes for heights between 2 and 5 m and 5 and 10 m (e.g., buttonwood), and red mangroves for the 15–20 m class.

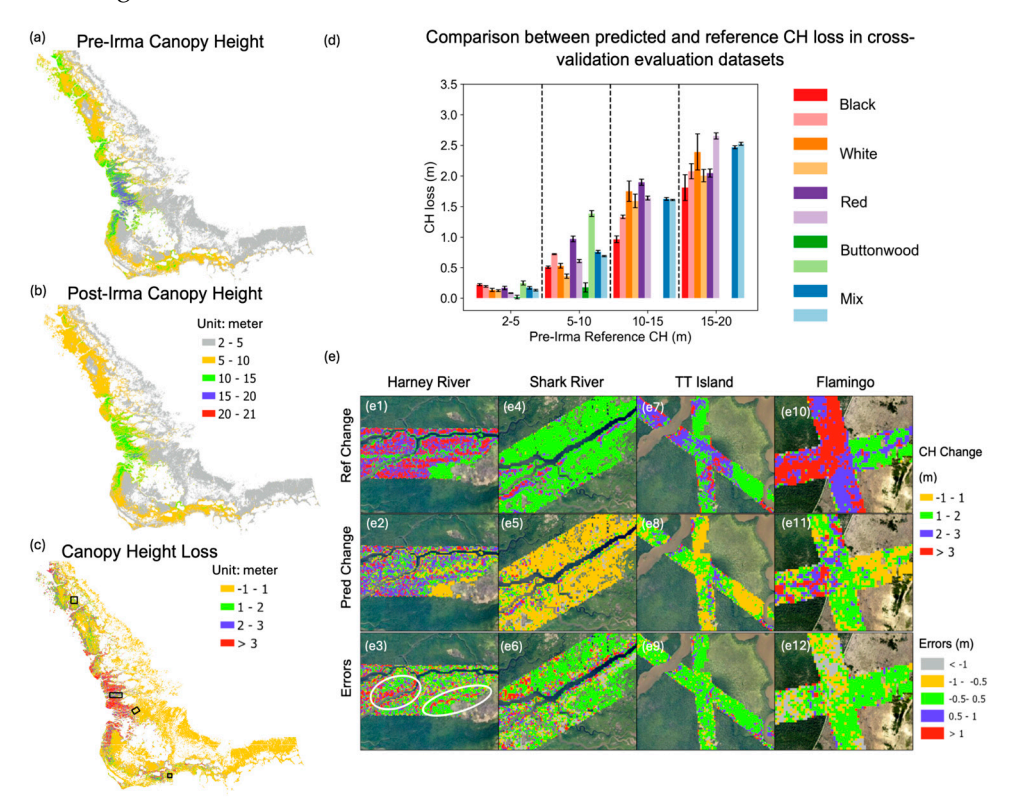


Figure 7. Predicted CH (a) pre-Irma, (b) post-Irma, and (c) CH loss (positive values indicate losses). (d) Comparison between mean and standard deviation of predicted and reference CH loss from evaluation datasets in cross-validation. Deep color represents predicted values and light color reference values. Missing data are due to no pixel samples. (e) Local maps of CH loss. White circles in (e3) indicate (left) the bank areas and (right) the boundary between white and red mangroves according to Figure 1f.

Regional CH maps resulting from the second model configuration showed pre-Irma tall mangroves were clustered around Harney River and Shark River with heights greater than 15 m (Figure 7a). Mangroves between 5 and 15 m were in the Ten Thousand Islands and Flamingo sites and short mangroves were located further inland. The post-Irma map showed shorter CHs for those located in Harney River and Shark River (Figure 7b).

Large areas with significant CH losses clustered along the coastline were not included in the coverage of the LiDAR footprint, i.e., the *DS2* area (Figure 7c). At a local scale, the predictions were accurate for most of the areas within the four selected sites (Figure 7e), but overestimation of CH loss occurred at the Harney River site along the banks of river channels and transition areas between taller red mangrove and shorter white mangroves at the southeastern corner of the site (Figures 1f,g and 7e3).

4.3. Results of Temporal Transfer Learning for CH Predictions

4.3.1. Comparison of CH Prediction Accuracy Between SAR and Optical Datasets

Without corrections, SAR datasets showed better results than optical and mixed observations (Table 4). Uncorrected CH predictions from SAR data were more accurate for tall trees over 10m compared to optical results (Table 5, Figure 8). However, SAR predictions overestimated the CH for shorter mangroves and were less accurate than optical predictions. For corrected predictions, the mix dataset achieved the highest accuracy with an RMSE of 1.80 m. Error correction models and prediction uncertainties were similar across species

classes (Figures S5 and S6). Using either the mean value of backscatter (RMSE = 4.1m) or a single backscatter value (RMSE = 4.1m), coupled with L3 classification and optical data, resulted in lower accuracy than using backscatter time series and L3 data (RMSE = 3.5 m).

Table 4. Mean and standard deviation values of accuracy parameters for predicted and corrected post-Irma CH.

Sensors	RMSE (m)		R	²
	Predicted	Corrected	Predicted	Corrected
SAR	3.5 ± 0.0	2.6 ± 0.0	0.5 ± 0.0	0.7 ± 0.0
Optical	4.1 ± 0.0	2.0 ± 0.0	0.2 ± 0.0	0.8 ± 0.0
Mix	4.1 ± 0.0	1.8 ± 0.0	0.2 ± 0.0	0.8 ± 0.0

Table 5. Uncorrected and corrected CH predictions RMSE (m) using different sensors across height classes.

	Uncorrected			Corrected		
	SAR	Optical	Mix	SAR	Optical	Mix
2–5 m	3.6	1.8	2.0	2.7	1.7	2.0
5–10 m	3.9	2.2	2.3	2.7	1.7	1.8
10–15 m	2.3	6.2	6.0	2.1	2.2	1.6
15–20 m	2.9	9.7	9.5	2.5	3.5	1.7

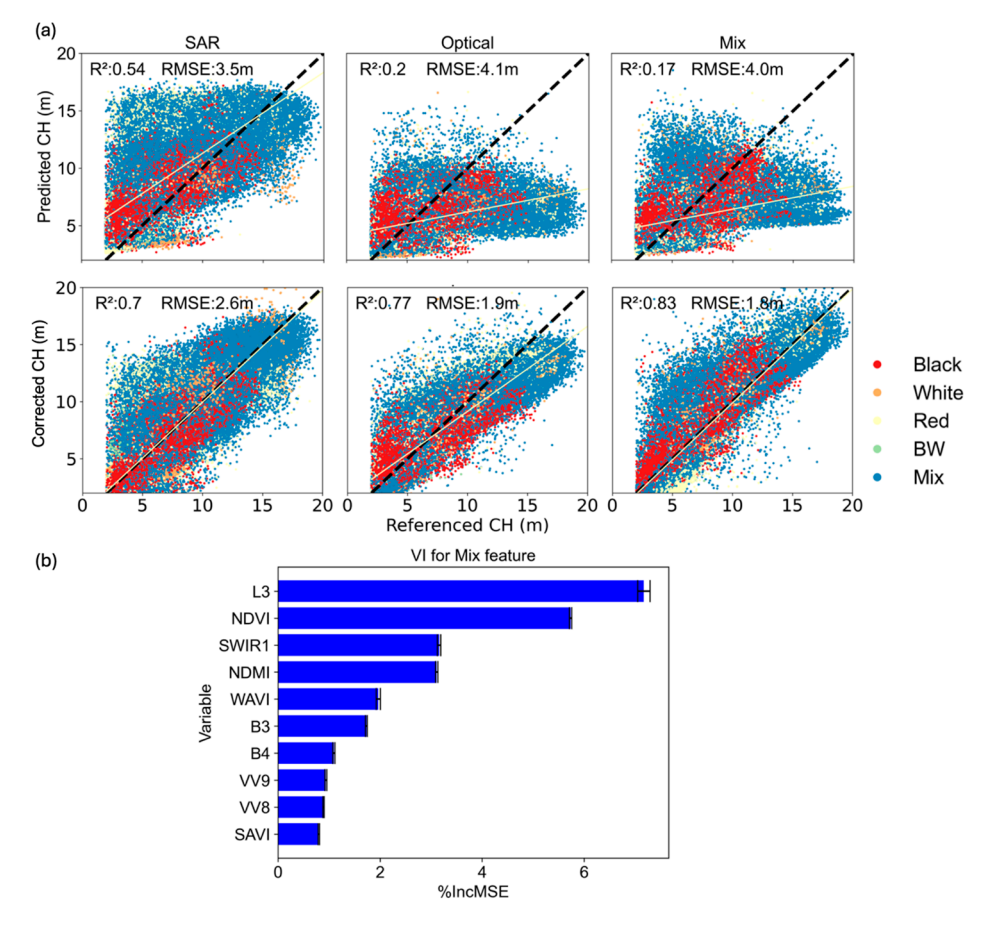


Figure 8. (a) Scatter plot of predicted and corrected CH versus reference post-Irma CH from a cross-validation dataset. (b) Mean and standard deviation of top ten ranking of variable importance using mixed features.

Remote Sens. 2024, 16, 3992 14 of 21

When using the mixed dataset, L3 classification was the most important variable, followed by optical and SAR variables. The importance of VV variables was consistently higher than VH variables. Overall, the importance ranking for each feature was consistent across the cross-validations with a minimal standard deviation.

4.3.2. Canopy Height and Height Loss Predictions

Corrected predictions for the entire *DS2* area showed the highest overall accuracy using the mixed features across height classes, except for the pre-Irma 2–5 m class, where the optical dataset achieved the best accuracy. By merging the mixed and optical results, we achieved an overall RMSE of 1.7 m. The spatial distribution of post-Irma CH predictions within the four sites was consistent with the reference values (Figure 9a–1). However, large errors clustered in the transition between tall red mangroves and short white mangroves in the Harney River site and along the banks of Shark River (Figure 9c,f).

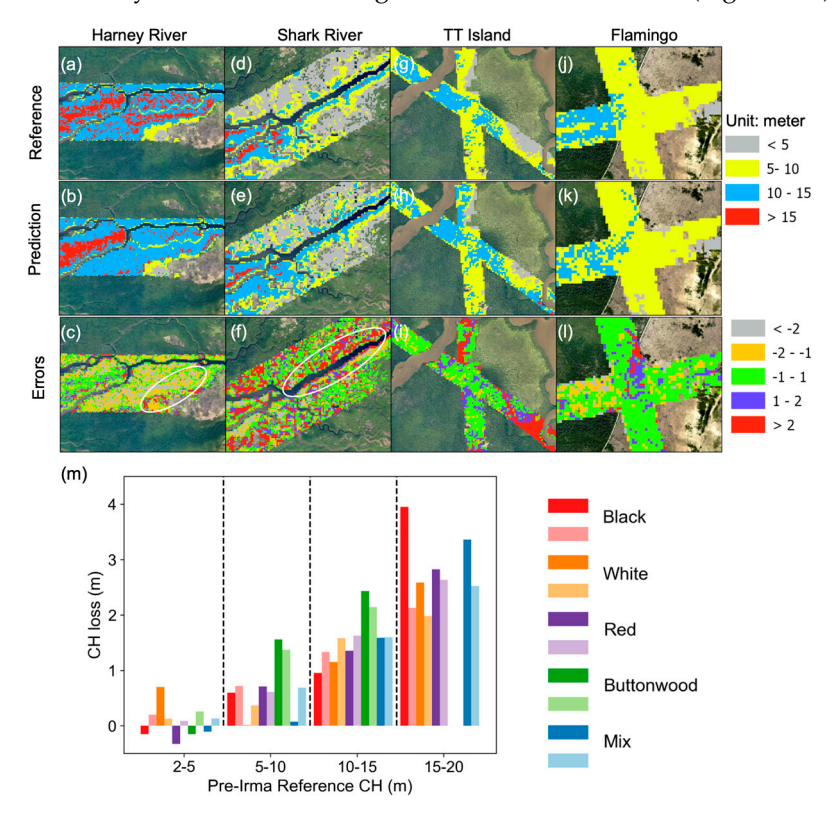


Figure 9. (a–l) Local maps of post-Irma CH reference, corrected predictions, and errors. White circle outlines indicate areas with large errors. (m) Comparison of the corrected predictions and reference CH losses across pre-Irma canopy height and species classes. Deep color indicates predicted values and light color reference values.

CH loss predictions calculated using the LiDAR pre-Irma CH and the corrected post-Irma CH values were overall comparable with reference values across height and species classes (Figure 9m). Most of the species/height classes had ratios of mean errors to reference CH loss less than 20%, except for some species classes for 0–5 m and 15–20 m. In particular, the black and mixed species for the 15–20 m height class showed higher ratio values.

5. Discussion

This study applied RF models to predict regional mangrove CH based on freely and openly available airborne LiDAR, spaceborne SAR and optical observations, and vegetation maps. This section discusses the complementary values of SAR backscatter and optical data in predicting CH for both spatial (Section 5.1) and temporal (Section 5.2) transfer learning. Each section explains varying prediction accuracy among height and species classes under

Remote Sens. 2024, 16, 3992 15 of 21

pre- and post-disturbance scenarios. Next, we compare the CH map products with similar studies (Section 5.3). Last, we discuss the limitations of the application of SAR and optical data for CH prediction (Section 5.4).

5.1. Spatial Transfer Learning

5.1.1. Performance Comparison of CH Predictions of SAR and Optical Models

The value of spatial transfer learning lies in predicting canopy height (CH) in areas where ground reference data are unavailable. Spatial transfer learning with SAR and optical observations complements each other during pre- and post-disturbance periods. Under the pre-disturbance leaf-on condition, CH predictions from SAR were not as accurate as optical across height classes, especially for the tall trees, because the penetration of microwave energy transmitted from radar is limited beneath the canopy layer. However, optical observations, especially vegetation indices, are sensitive to properties of leaf area, which correlates with CH. Under post-disturbance conditions with predominantly leaf-off vegetation, CH predictions from SAR were more accurate than optical predictions because the deeper penetration level of microwave energy, and thus, the backscatter, is more sensitive to woody components [57]. For the optical sensor, the lack of foliage significantly reduces the amount of reflected light from the canopy, making it difficult to predict forest structure [58]. We evaluated correlations between backscatter data and tidal gauges, which further supported this explanation (Note S2 and Figure S7). We suggest that SAR features are more effective for predicting mangrove CH when the canopy is relatively open, while optical features are more effective for dense canopies. Backscatter time series coupled with optical features yielded higher accuracy than using only single sensor data, which aligns with previous studies [59]. Since using a single backscatter value achieved only slightly less accuracy than using the time series, we propose that a SAR time series is not necessary for spatial transfer learning.

When using the mixed feature datasets, optical indices were overall more important than SAR variables for pre-Irma, whereas the importance of some SAR variables increased for the post-Irma period. High importance of the vegetation information (L3) variable is attributed to the spatial distribution of the L3 classes, which changes from "Mangrove Forest" class to "Mangrove Shrub" and "Mangrove Scrub" classes from the coastline to inland. This pattern is associated with the spatial variation of CH as heights decrease with increasing distance from the coastline (Figure 1b, [15]). The variable importances for SAR and optical features were consistent in the cross-validation tests with minimal standard deviations (Figure 5b), suggesting the robustness and generalizability of the model's feature selection process to consistently select the same significant features across cross-validation tests. We suggest that when both SAR and optical observations are available, there is no need to only use a subset of the most important features because it does not perform as well as using all available features. For the post-disturbance condition, we suggest using SAR for spatial transfer learning when cloud-free optical imagery is not available.

5.1.2. Accuracy Assessment of CH Loss

Estimated CH loss achieved high accuracy by canceling out pre- and post-disturbance errors in CH estimates due to the similar linear relationship between prediction errors and reference CH across periods for each species (Figures 6 and 7). These linear relationships were linked to the growth forms of mangrove trees, which are determined by species. CH loss is higher for taller trees, but the variations in loss were relatively homogeneous across species. The predictions for the evaluation datasets showed high accuracy across height and species classes, which heightens confidence of reliable CH loss estimates for the study area beyond the LiDAR footprint (Figure 7d). Low accuracy of height loss predictions was found along river channels and at the transition between different species (Figure 7(e3)), where 30 m pixels are more likely to encompass water surfaces and multiple species that affect SAR backscatter and optical reflectance values differently.

5.2. Temporal Transfer Learning

5.2.1. Comparison of the Performance of CH Predictions Between SAR and Optical Models

The value of temporal transfer learning lies in predicting CH after a natural disturbance within a practical timeframe using pre-disturbance data. Uncorrected post-Irma CH predictions from backscatter time series showed higher accuracy than optical and mixed datasets (Figure 8) without saturation in height prediction, because differences in pre- and post-Irma backscatter indicate changes in woody components. In particular, for the tallest trees with 15–20 m pre-Irma height, predictions from the backscatter series achieved 2.9 m RMSE without any correction because backscatter represents the structure of the canopy and trunk layer of the forests. In contrast, optical predictions were saturated at about 10 m and cannot be used for tall mangroves. Using backscatter time series achieved better results than using a single backscatter image coupled with optical data because a time series, representing the tidal water variations, provides more data for the model to select the most useful variables for CH prediction. Our study proves that radar is a useful tool to estimate post-disturbance CH for tall trees.

However, uncorrected SAR predictions overestimated CH of short mangroves (Table 5). Changes in SAR backscatter, other than tree height, are likely related to storm-derived sediment deposition and erosion, woody debris accumulations, changes in water surface caused by storm surge, and high precipitation [9–11,36,37,60] (Figures 4b and S3). In contrast, optical features achieved high accuracy for short mangroves located farther from the coastline with less branch damage and defoliation (e.g., the buttonwood example in Figure 4b) where observed values were similar between pre- and post-disturbance.

Considering the complementary properties of SAR and optical results, uncorrected predictions from them can be used collectively, i.e., using optical predictions for short mangroves and SAR predictions for tall mangroves. We achieved an overall RMSE of 2.2 m using the uncorrected optical predictions when pre-Irma CH is less than 10 m and using SAR predictions when pre-Irma CH is greater than 10 m. This accuracy was close to the RMSE with corrected predictions (1.7 m).

5.2.2. Accuracy Assessment of CH Loss

Temporal transfer learning coupled with error modeling proves to be an efficient tool to accurately predict post-disturbance CH. Though CH loss predictions were comparable to reference data across all species and height classes, bias existed for black mangrove within the 15–20 m height class (Figure 9m). It can be attributed to the pneumatophores, a distinctive aerial root of black mangroves protruding above the soil or water surface, affecting the reflectance values of both radar and optical signals. In addition, large errors were encountered in areas with heterogenous vegetation and exposed water surfaces and soil, for example, along river banks or at transition boundaries between two mangrove species. The 30 m resolution observations include multiple surface elements, resulting in lower accuracy.

5.3. Comparison with Previous Studies on the South Florida Mangrove CH

We compared our maps of absolute CH and CH loss with two previous relevant studies by Jamaluddin et al. (2024) and Lagomasino et al. (2021) [10,32]. These studies calculated pre- and post-Irma CH and losses for the mangroves in South Florida using the same G-LiHT datasets for reference as our study.

5.3.1. Comparison of Regional Pre-Irma CH

We compared the regional pre-Irma mangrove CH predictions with Jamaluddin et al. (2024) who used a deep learning convolutional long short-term memory (ConvLSTM) and transformer model (SST-CLT, Figure 10a,b) [32]. In a similar approach, they used the pre-Irma G-LiHT CHMs as labels to calibrate models with Sentinel-1 SAR and Sentinel-2 optical features, resulting in an RMSE of 2.47 m and MAE of 1.92 m. For comparison, we achieved an RMSE of 1.93 m and MAE of 1.38 m by including mangrove class information but

Remote Sens. 2024, 16, 3992 17 of 21

using a simpler classifier model RF. The deep learning model requires more sophisticated training on the model network and hyperparameter optimization. We thus recommend employing the RF model in conjunction with vegetation class information if available due to its improved prediction accuracy.

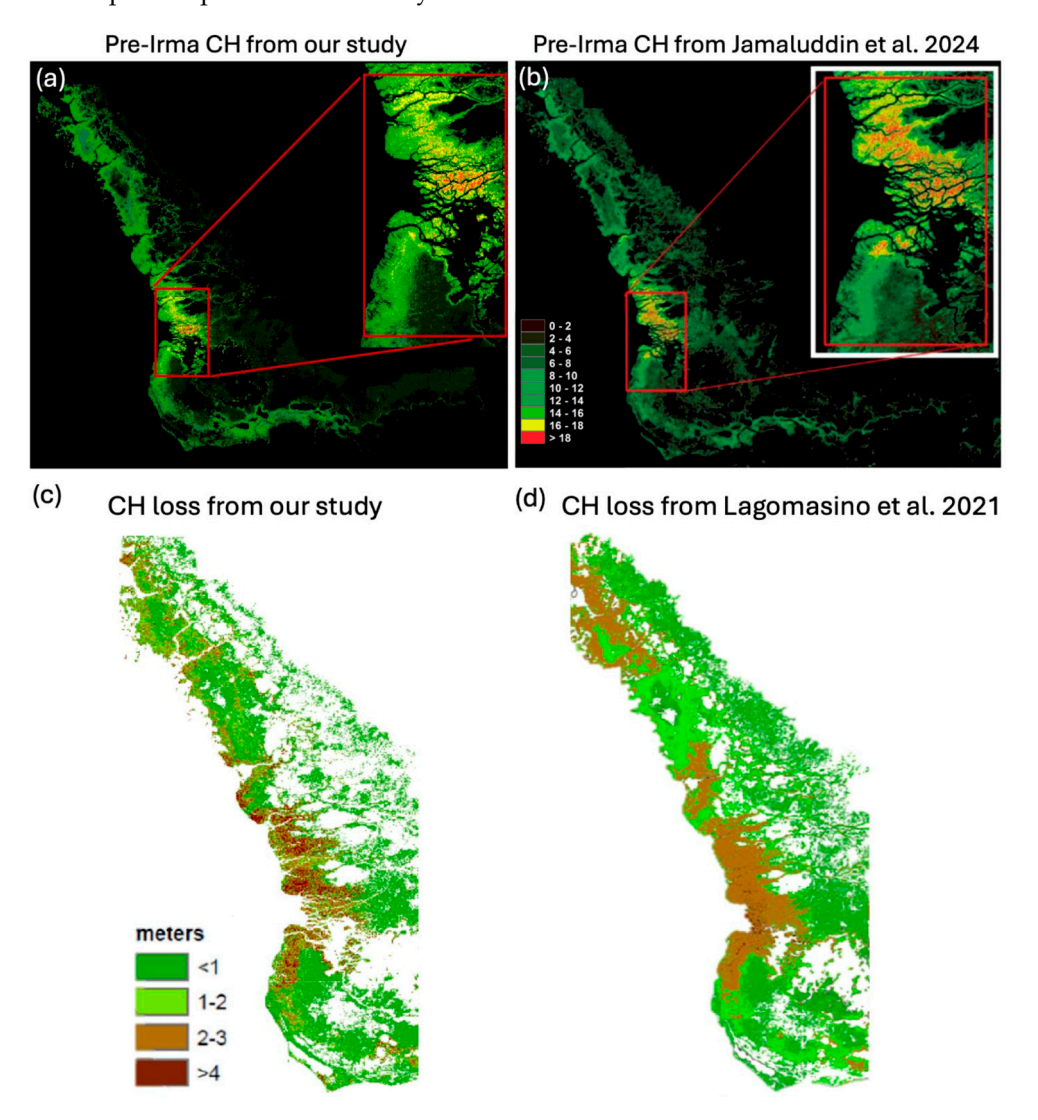


Figure 10. (a,b) Pre-Irma CH maps for (a) remake of Figure 7a and (b) Figure from Jamaluddin et al. (2024) [32]. (c) Remake of CH loss predictions from Figure 7c. (d) CH loss predictions from Lagomasino et al. (2021) [10].

Both studies showed a consistent spatial pattern of CH, whereas discrepancies occurred at the coastal area with tall mangroves (red frames in Figure 10a,b). However, it may require external in situ height measurements or LiDAR data to verify which product is more accurate.

5.3.2. Comparison of Regional CH Loss

Lagomasino et al. (2021) estimated pre-Irma CH for South Florida mangrove ecosystems using commercial satellite WorldView-2 stereo imagery and calibrated the results with G-LiHT data. Post-Irma CH was modelled using pre-Irma CH and max wind speed [10]. While this study aligns with our spatial transfer learning results, showing that taller mangroves generally experience higher losses (Figure 7c), Lagomasino et al. (2021) predicted less magnitude of CH losses for tall mangroves around the western central coastline, but greater losses in the Ten Thousand Islands (Figure 10c,d). The discrepancies might be

Remote Sens. 2024, 16, 3992 18 of 21

attributed to the pre-Irma CH predictions with WorldView-2 stereo images acquired in 2012–2013, 4–5 years before Hurricane Irma. Moreover, the wind speed model product that was used for post-Irma CH modelling had a resolution of 5 km, which may impact accuracy at short distances along coasts and open water ways. In addition, our loss map, derived from spatial transfer learning models, might be biased by training data availability not covering the full range of canopy heights and height loss.

5.4. Limitations

There are several limitations of using SAR data including their sensitivity to tidal water levels. Future studies need to investigate the relationship between tidal water levels and SAR backscatter, which can support selecting backscatter time series elements for CH prediction. In addition, variations in the SAR incidence angle across the swath can impact the backscatter value and performance of spatial transfer learning. However, it may have little impact on the temporal transfer learning because the incidence angles for the same location were consistent over time.

Moreover, the accuracy of spatial transfer learning cannot be quantified for areas outside the reference data footprint, which requires external measurements to evaluate the results from different studies. To increase the model accuracy, future studies can train models among various sites with distinct inundation frequency and depth.

Finally, changes in SAR and optical values due to phenological changes in vegetation [61] can affect the accuracy of temporal transfer learning. Dense and tall mangroves in South Florida were observed in November and December when leaf area index is the highest, resulting in the highest NDVI values in a year [22]. Future studies should prioritize using spaceborne observations from the same season for temporal transfer learning.

6. Conclusions

Damages from natural disturbance often occur over large spatial extents, and the availability of large extent datasets before and after disturbances is crucial for an effective assessment of damage magnitude and location. LiDAR data provide the highest accuracy of canopy height models to date, but they are expensive and time consuming to acquire. This study calibrated RF models for spatial and temporal transfer learning to predict regional pre- and post-Hurricane Irma mangrove CH in South Florida using SAR and optical observations in combination with mangrove class information. We found critical insights on the complementary values of both sensors in CH prediction. For spatial transfer learning, the performance of the SAR and optical models varied between preand post-disturbance periods. Optical data showed higher accuracy than SAR for predisturbance leaf-on conditions, while SAR outperformed optical data in post-disturbance leaf-off conditions. Fusing data from both sensors yielded the highest accuracy with an overall RMSE of 1.93 m and 1.80 m for pre- and post-disturbance periods. CH loss predictions achieved reasonable accuracy across height classes. Spatial transfer learning discovered areas with CH losses exceeding 2 m along the central western coastline, where only limited LiDAR samples were available.

Temporal transfer learning models predict post-disturbance CH using models calibrated by pre-disturbance data. SAR predictions were more accurate than optical results for tall mangroves over 10 m and optical predictions were more accurate for shorter mangroves. We applied a species-specific linear model for error correction and accomplished an RMSE of 1.70 m. In particular, a SAR backscatter time series achieves greater accuracy than a single acquisition for temporal transfer learning, but their results were comparable for spatial transfer learning. We propose that, for future hurricane events, the post-disturbance CH can be estimated by fusing the SAR and optical uncorrected temporal transfer learning predictions based on pre-disturbance CH, which can lead to reasonable estimates.

With the projected increase in the frequency of major hurricanes due to climate change, the aftermath of Hurricane Irma offered a unique chance to explore the application of publicly available remote sensing data in assessing canopy structure damages. The spatial and

temporal transfer learning methods provide key information for conservation managers to evaluate impacts and changes in carbon storage, loss, and uptake capacity over large areas following a disturbance within a reasonable timeframe. The study provides a foundation for future research aimed at understanding mangrove dynamics on a global scale and investigating mangrove damages and recovery patterns over time.

Supplementary Materials: The following supporting information can be downloaded at: https://www.mdpi.com/article/10.3390/rs16213992/s1.

Author Contributions: Conceptualization, B.Z. and D.G.; data curation, B.Z.; formal analysis, B.Z. and D.G.; funding acquisition, S.W.; investigation, B.Z., L.L.-W., K.S.I. and K.S.; methodology, B.Z., D.G., S.W., C.L. and E.H.; project administration, E.H. and Y.L.; resources, B.Z., L.L.-W., K.S.I., K.S. and Y.L.; software, B.Z., D.G., C.L. and K.S.; supervision, B.Z., D.G., and S.W.; validation, B.Z. and C.L.; visualization, B.Z.; writing—original draft, B.Z.; writing—review and editing, B.Z., D.G., S.W., C.L., E.H., L.L.-W. and K.S.I. All authors have read and agreed to the published version of the manuscript.

Funding: This research was conducted as part of the Florida Coastal Everglades Long-Term Ecological Research program funded by the NSF Rapid Grant DEB-18012244. This is publication number 1783 from the Institute of Environment at Florida International University.

Data Availability Statement: The data presented in this study are available on request from the corresponding author due to the large size of the datasets. The machine learning model scripts are provided in a GitHub repository: https://github.com/gannd/SAR_transfer_learner.git.

Acknowledgments: We thank NASA G-LiHT program for providing the pre- and post-hurricane canopy height model data. We also thank the European Space Agency and Alaska Satellite Facility for providing the Sentinel-1 data. We acknowledge Selena Chavez for her help with obtaining G-LiHT CHM data and the Coastlines and Oceans Division at Florida International University for their support.

Conflicts of Interest: All authors declare that the research was conducted in the absence of any commercial or financial relationships that could be construed as a potential conflict of interest.

References

- 1. Donato, D.C.; Kauffman, J.B.; Murdiyarso, D.; Kurnianto, S.; Stidham, M.; Kanninen, M. Mangroves among the Most Carbon-Rich Forests in the Tropics. *Nat. Geosci.* **2011**, *4*, 293–297. [CrossRef]
- 2. Giri, C.; Ochieng, E.; Tieszen, L.L.; Zhu, Z.; Singh, A.; Loveland, T.; Masek, J.; Duke, N. Status and Distribution of Mangrove Forests of the World Using Earth Observation Satellite Data. *Glob. Ecol. Biogeogr.* **2011**, 20, 154–159. [CrossRef]
- 3. Fatoyinbo, T.; Feliciano, E.A.; Lagomasino, D.; Lee, S.K.; Trettin, C. Estimating Mangrove Aboveground Biomass from Airborne LiDAR Data: A Case Study from the Zambezi River Delta. *Environ. Res. Lett.* **2018**, *13*, 025012. [CrossRef]
- 4. Wilkie, M.L.; Fortuna, S. Status and Trends in Mangrove Area Extent Worldwide; Forestry Department, Food and Agriculture Organization of the United Nations: Rome, Italy, 2003.
- 5. Mithapala, S. *Mangroves: Coastal Ecosystem Series*; IUCN Ecosystems and Livelihoods Group Asia: Colombo, Sri Lanka, 2008; Volume 2.
- 6. International Union for Conservation of Nature (IUCN) Red List of Ecosystems, More Than Half of All Mangrove Ecosystems at Risk of Collapse by 2050, First Global Assessment Finds. 2024. Available online: https://www.iucn.org/press-release/202405/more-half-all-mangrove-ecosystems-risk-collapse-2050-first-global-assessment (accessed on 5 July 2024).
- 7. Goldberg, L.; Lagomasino, D.; Thomas, N.; Fatoyinbo, T. Global Declines in Human-Driven Mangrove Loss. *Glob. Change Biol.* **2020**, *26*, 5844–5855. [CrossRef] [PubMed]
- 8. Simard, M.; Zhang, K.; Rivera-Monroy, V.H.; Ross, M.S.; Ruiz, P.L.; Castañeda-Moya, E.; Twilley, R.R.; Rodriguez, E. Mapping Height and Biomass of Mangrove Forests in Everglades National Park with SRTM Elevation Data. *Photogramm. Eng. Remote Sens.* **2006**, 72, 299–311. [CrossRef]
- 9. Castañeda-Moya, E.; Rivera-Monroy, V.H.; Chambers, R.M.; Zhao, X.; Lamb-Wotton, L.; Gorsky, A.; Gaiser, E.E.; Troxler, T.G.; Kominoski, J.S.; Hiatt, M. Hurricanes Fertilize Mangrove Forests in the Gulf of Mexico (Florida Everglades, USA). *Proc. Natl. Acad. Sci. USA* **2020**, *117*, 4831–4841. [CrossRef]
- Lagomasino, D.; Fatoyinbo, T.; Castañeda-Moya, E.; Cook, B.D.; Montesano, P.M.; Neigh, C.S.R.; Corp, L.A.; Ott, L.E.; Chavez, S.; Morton, D.C. Storm Surge and Ponding Explain Mangrove Dieback in Southwest Florida Following Hurricane Irma. *Nat. Commun.* 2021, 12, 4003. [CrossRef]
- 11. Chavez, S.; Wdowinski, S.; Lagomasino, D.; Castañeda-Moya, E.; Fatoyinbo, T.; Moyer, R.P.; Smoak, J.M. Estimating Structural Damage to Mangrove Forests Using Airborne Lidar Imagery: Case Study of Damage Induced by the 2017 Hurricane Irma to Mangroves in the Florida Everglades, USA. *Sensors* 2023, 23, 6669. [CrossRef]

12. Komiyama, A.; Poungparn, S.; Kato, S. Common Allometric Equations for Estimating the Tree Weight of Mangroves. *J. Trop. Ecol.* **2005**, 21, 471–477. [CrossRef]

- 13. Lefsky, M.A. A Global Forest Canopy Height Map from the Moderate Resolution Imaging Spectroradiometer and the Geoscience Laser Altimeter System. *Geophys. Res. Lett.* **2010**, 37. [CrossRef]
- 14. Simard, M.; Pinto, N.; Fisher, J.B.; Baccini, A. Mapping forest canopy height globally with spaceborne lidar. *J. Geophys. Res. Biogeosci.* **2011**, *116*. [CrossRef]
- 15. Xiong, L.; Lagomasino, D.; Charles, S.P.; Castañeda-Moya, E.; Cook, B.D.; Redwine, J.; Fatoyinbo, L. Quantifying Mangrove Canopy Regrowth and Recovery after Hurricane Irma with Large-Scale Repeat Airborne Lidar in the Florida Everglades. *Int. J. Appl. Earth Obs. Geoinf.* 2022, 114, 103031. [CrossRef]
- 16. Ghosh, S.M.; Behera, M.D.; Paramanik, S. Canopy Height Estimation Using Sentinel Series Images through Machine Learning Models in a Mangrove Forest. *Remote Sens.* 2020, 12, 1519. [CrossRef]
- 17. Hollaus, M.; Wagner, W.; Eberhöfer, C.; Karel, W. Accuracy of Large-Scale Canopy Heights Derived from LiDAR Data under Operational Constraints in a Complex Alpine Environment. *ISPRS J. Photogramm. Remote Sens.* **2006**, *60*, 323–338. [CrossRef]
- 18. Li, W.; Niu, Z.; Shang, R.; Qin, Y.; Wang, L.; Chen, H. High-Resolution Mapping of Forest Canopy Height Using Machine Learning by Coupling ICESat-2 LiDAR with Sentinel-1, Sentinel-2 and Landsat-8 Data. *Int. J. Appl. Earth Obs. Geoinf.* **2020**, 92, 102163. [CrossRef]
- 19. Potapov, P.; Li, X.; Hernandez-Serna, A.; Tyukavina, A.; Hansen, M.C.; Kommareddy, A.; Pickens, A.; Turubanova, S.; Tang, H.; Silva, C.E.; et al. Mapping Global Forest Canopy Height through Integration of GEDI and Landsat Data. *Remote Sens. Environ.* **2021**, 253, 112165. [CrossRef]
- 20. Zhang, K. Identification of Gaps in Mangrove Forests with Airborne LIDAR. *Remote Sens. Environ.* **2008**, 112, 2309–2325. [CrossRef]
- 21. Leitold, V.; Morton, D.C.; Martinuzzi, S.; Paynter, I.; Uriarte, M.; Keller, M.; Ferraz, A.; Cook, B.D.; Corp, L.A.; González, G. Tracking the Rates and Mechanisms of Canopy Damage and Recovery Following Hurricane Maria Using Multitemporal Lidar Data. *Ecosystems* 2022, 25, 892–910. [CrossRef]
- 22. Zhang, K.; Thapa, B.; Ross, M.; Gann, D. Remote Sensing of Seasonal Changes and Disturbances in Mangrove Forest: A Case Study from South Florida. *Ecosphere* **2016**, 7, e01366. [CrossRef]
- 23. Han, X.; Feng, L.; Hu, C.; Kramer, P. Hurricane-induced Changes in the Everglades National Park Mangrove Forest: Landsat Observations between 1985 and 2017. *J. Geophys. Res. Biogeosci.* **2018**, 123, 3470–3488. [CrossRef]
- 24. Zhang, C.; Durgan, S.D.; Lagomasino, D. Modeling Risk of Mangroves to Tropical Cyclones: A Case Study of Hurricane Irma. Estuar. Coast. *Shelf Sci.* **2019**, 224, 108–116. [CrossRef]
- 25. Taillie, P.J.; Roman-Cuesta, R.; Lagomasino, D.; Cifuentes-Jara, M.; Fatoyinbo, T.; Ott, L.E.; Poulter, B. Widespread Mangrove Damage Resulting from the 2017 Atlantic Mega Hurricane Season. *Environ. Res. Lett.* **2020**, *15*, 064010. [CrossRef]
- 26. Joshi, N.P.; Mitchard, E.T.A.; Schumacher, J.; Johannsen, V.K.; Saatchi, S.; Fensholt, R. L-Band SAR Backscatter Related to Forest Cover, Height and Aboveground Biomass at Multiple Spatial Scales across Denmark. *Remote Sensing* **2015**, *7*, 4442–4472. [CrossRef]
- 27. Sinha, S.; Jeganathan, C.; Sharma, L.K.; Nathawat, M.S. A Review of Radar Remote Sensing for Biomass Estimation. *Int. J. Environ. Sci. Technol.* **2015**, 12, 1779–1792. [CrossRef]
- 28. Lucas, R.; Van De Kerchove, R.; Otero, V.; Lagomasino, D.; Fatoyinbo, L.; Omar, H.; Satyanarayana, B.; Dahdouh-Guebas, F. Structural Characterisation of Mangrove Forests Achieved through Combining Multiple Sources of Remote Sensing Data. *Remote Sens. Environ.* 2020, 237, 111543. [CrossRef]
- 29. Hyde, P.; Dubayah, R.; Walker, W.; Blair, J.B.; Hofton, M.; Hunsaker, C. Mapping Forest Structure for Wildlife Habitat Analysis Using Multi-Sensor (LiDAR, SAR/InSAR, ETM+, Quickbird) Synergy. *Remote Sens. Environ.* **2006**, 102, 63–73. [CrossRef]
- 30. Xi, Z.; Xu, H.; Xing, Y.; Gong, W.; Chen, G.; Yang, S. Forest Canopy Height Mapping by Synergizing ICESat-2, Sentinel-1, Sentinel-2 and Topographic Information Based on Machine Learning Methods. *Remote Sens.* **2022**, *14*, 364. [CrossRef]
- 31. García, M.; Saatchi, S.; Ustin, S.; Balzter, H. Modelling Forest Canopy Height by Integrating Airborne LiDAR Samples with Satellite Radar and Multispectral Imagery. *Int. J. Appl. Earth Obs. Geoinf.* **2018**, *66*, 159–173. [CrossRef]
- 32. Jamaluddin, I.; Chen, Y.-N.; Fan, K.-C. Spatial–Spectral–Temporal Deep Regression Model With Convolutional Long Short-Term Memory and Transformer for the Large-Area Mapping of Mangrove Canopy Height by Using Sentinel-1 and Sentinel-2 Data. *IEEE Trans. Geosci. Remote Sens.* **2024**, *62*, 4403117. [CrossRef]
- 33. Zhang, B.; Smith, K.; Wdowinski, S.; Lin, C.; Gann, D.; Chavez, S.; Zhang, J. Space-Based Mapping of Mangrove Canopy Height with Multi-Sensor Observations and Deep Learning Techniques. In Proceedings of the IGARSS 2022—2022 IEEE International Geoscience and Remote Sensing Symposium, Kuala Lumpur, Malaysia, 17–22 July 2022; pp. 3389–3392.
- 34. Chen, L.; Lin, H.; Long, J.; Liu, Z.; Yang, P.; Zhang, T. Evaluating the Transferability of Spectral Variables and Prediction Models for Mapping Forest Aboveground Biomass Using Transfer Learning Methods. *Remote Sens.* **2023**, *15*, 5358. [CrossRef]
- 35. Pflugmacher, D.; Cohen, W.B.; Kennedy, R.E. Using Landsat-Derived Disturbance History (1972–2010) to Predict Current Forest Structure. *Remote Sens. Environ.* **2012**, 122, 146–165. [CrossRef]
- 36. Zhang, B.; Wdowinski, S.; Gann, D. Space-Based Detection of Significant Water-Depth Increase Induced by Hurricane Irma in the Everglades Wetlands Using Sentinel-1 SAR Backscatter Observations. *Remote Sens.* **2022**, *14*, 1415. [CrossRef]

37. Zhang, B.; Wdowinski, S.; Gann, D.; Hong, S.-H.; Sah, J. Spatiotemporal Variations of Wetland Backscatter: The Role of Water Depth and Vegetation Characteristics in Sentinel-1 Dual-Polarization SAR Observations. *Remote Sens. Environ.* **2022**, 270, 112864. [CrossRef]

- 38. Chen, R.; Twilley, R.R. Patterns of Mangrove Forest Structure and Soil Nutrient Dynamics along the Shark River Estuary, Florida. Estuaries 1999, 22, 955. [CrossRef]
- 39. Twilley, R.R.; Rivera-Monroy, V.H. Developing Performance Measures of Mangrove Wetlands Using Simulation Models of Hydrology, Nutrient Biogeochemistry, and Community Dynamics. *J. Coast. Res.* **2005**, 79–93.
- 40. Castañeda-Moya, E.; Twilley, R.R.; Rivera-Monroy, V.H. Allocation of Biomass and Net Primary Productivity of Mangrove Forests along Environmental Gradients in the Florida Coastal Everglades, USA. *For. Ecol. Manag.* **2013**, 307, 226–241. [CrossRef]
- 41. Feliciano, E.A.; Wdowinski, S.; Potts, M.D.; Lee, S.-K.; Fatoyinbo, T.E. Estimating Mangrove Canopy Height and Above-Ground Biomass in the Everglades National Park with Airborne LiDAR and TanDEM-X Data. *Remote Sens.* **2017**, *9*, 702. [CrossRef]
- 42. Peereman, J.; Hogan, J.A.; Lin, T.-C.; Michaletz, S. Disturbance Frequency, Intensity and Forest Structure Modulate Cyclone-induced Changes in Mangrove Forest Canopy Cover. *Glob. Ecol. Biogeogr.* **2022**, *31*, 37–50. [CrossRef]
- 43. Cook, B.D.; Corp, L.A.; Nelson, R.F.; Middleton, E.M.; Morton, D.C.; McCorkel, J.T.; Masek, J.G.; Ranson, K.J.; Ly, V.; Montesano, P.M. NASA Goddard's LiDAR, Hyperspectral and Thermal (G-LiHT) Airborne Imager. *Remote Sens.* **2013**, *5*, 4045–4066. [CrossRef]
- 44. Zhang, C. Multi-Sensor System Applications in the Everglades Ecosystem; CRC Press: Boca Raton, FL, USA, 2020.
- 45. Ruiz, P.L.; Schall, T.N.; Shamblin, R.B.; Whelan, K.R.T. *The Vegetation of Everglades National Park: Final Report*; Natation Resource Report NPS/SFCN/NRR—2021/2256; National Park Service: Fort Collins, CO, USA, 2021.
- 46. Filipponi, F. Sentinel-1 GRD Preprocessing Workflow. Proceedings 2019, 18, 11. [CrossRef]
- 47. Inglada, J.; Vincent, A.; Arias, M.; Marais-Sicre, C. Improved Early Crop Type Identification By Joint Use of High Temporal Resolution SAR And Optical Image Time Series. *Remote Sens.* **2016**, *8*, 362. [CrossRef]
- 48. Radabaugh, K.R.; Moyer, R.P.; Chappel, A.R.; Dontis, E.E.; Russo, C.E.; Joyse, K.M.; Bownik, M.W.; Goeckner, A.H.; Khan, N.S. Mangrove Damage, Delayed Mortality, and Early Recovery Following Hurricane Irma at Two Landfall Sites in Southwest Florida, USA. Estuaries Coasts 2020, 43, 1104–1118. [CrossRef]
- 49. Gorelick, N.; Hancher, M.; Dixon, M.; Ilyushchenko, S.; Thau, D.; Moore, R. Google Earth Engine: Planetary-Scale Geospatial Analysis for Everyone. *Remote Sens. Environ.* **2017**, 202, 18–27. [CrossRef]
- 50. Rouse, J.W.; Haas, R.H.; Schell, J.A.; Deering, D.W. Monitoring vegetation systems in the Great Plains with ERTS. *NASA Spec. Publ.* **1974**, *351*, 309.
- 51. Gao, B.-C. NDWI—A Normalized Difference Water Index for Remote Sensing of Vegetation Liquid Water from Space. *Remote Sens. Environ.* **1996**, *58*, 257–266. [CrossRef]
- 52. Huete, A.R. A Soil-Adjusted Vegetation Index (SAVI). Remote Sens. Environ. 1988, 25, 295–309. [CrossRef]
- 53. Villa, P.; Mousivand, A.; Bresciani, M. Aquatic Vegetation Indices Assessment through Radiative Transfer Modeling and Linear Mixture Simulation. *Int. J. Appl. Earth Obs. Geoinf.* **2014**, *30*, 113–127. [CrossRef]
- 54. Breiman, L. Random Forests. Mach. Learn. 2001, 45, 5–32. [CrossRef]
- 55. Kuhn, M. Building Predictive Models in R Using the Caret Package. J. Stat. Softw. 2008, 28, 1–26. [CrossRef]
- 56. Pal, M. Random Forest Classifier for Remote Sensing Classification. Int. J. Remote Sens. 2005, 26, 217–222. [CrossRef]
- 57. Kobayashi, S.; Fujita, M.S.; Omura, Y.; Matthews, J.P. Analysis of the Relationship between L-Band SAR Backscatter and Understory Weed Density in Eucalyptus Plantation Forests. *Glsci Remote Sens.* **2024**, *61*, 2360771. [CrossRef]
- 58. Yan, G.; Hu, R.; Luo, J.; Weiss, M.; Jiang, H.; Mu, X.; Xie, D.; Zhang, W. Review of Indirect Optical Measurements of Leaf Area Index: Recent Advances, Challenges, and Perspectives. *Agric. For. Meteorol.* **2019**, 265, 390–411. [CrossRef]
- 59. Shen, Z.; Miao, J.; Wang, J.; Zhao, D.; Tang, A.; Zhen, J. Evaluating Feature Selection Methods and Machine Learning Algorithms for Mapping Mangrove Forests Using Optical and Synthetic Aperture Radar Data. *Remote Sens.* **2023**, *15*, 5621. [CrossRef]
- 60. Zhang, B.; Wdowinski, S.; Oliver-Cabrera, T.; Koirala, R.; Jo, M.J.; Osmanoglu, B. Mapping the Extent and Magnitude of Sever Flooding Induced by Hurricane Irma with Multi-Temporal Sentinel-1 Sar and InSAR Observations. *ISPRS—Int. Arch. Photogramm. Remote Sens. Spat. Inf. Sci.* **2018**, XLII–3, 2237–2244. [CrossRef]
- 61. Zhang, B.; Hestir, E.; Yunjun, Z.; Reiter, M.; Viers, J.H.; Schaffer-Smith, D.; Sesser, K. Multi-Temporal Analysis of InSAR Coherence, NDVI, and in Situ Water Depths for Managed Wetlands in National Wildlife Refuges, California. In Proceedings of the IGARSS 2023—2023 IEEE International Geoscience and Remote Sensing Symposium, Pasadena, CA, USA, 16–21 July 2023; pp. 8186–8189.

Disclaimer/Publisher's Note: The statements, opinions and data contained in all publications are solely those of the individual author(s) and contributor(s) and not of MDPI and/or the editor(s). MDPI and/or the editor(s) disclaim responsibility for any injury to people or property resulting from any ideas, methods, instructions or products referred to in the content.